IBRACON Structures and Materials Journal
Revista IBRACON de Estruturas e Materiais
ISSN 1983-4195 ismj.org

ORIGINAL ARTICLE

Numerical simulation of punching shear in flat slabs with spherical voids subjected to symmetric and asymmetric loadings

Simulação numérica da punção em lajes lisas com vazios esféricos submetidas a carregamentos simétricos e assimétricos

Eric Renã Zavitzki Schimanowski[a]
Américo Campos Filho[a]
Bruna Manica Lazzari[a,b]
Paula Manica Lazzari[a]

[a]Universidade Federal do Rio Grande do Sul – UFRGS, Escola de Engenharia, Departamento de Engenharia Civil, Porto Alegre, RS, Brasil
[b]Pontifícia Universidade Católica do Rio Grande do Sul – PUC-RS, Escola Politécnica, Departamento de Engenharia Civil, Porto Alegre, RS, Brasil

Received 25 January 2024
Revised 07 April 2024
Accepted 14 May 2024

Abstract: Using hollow spherical voids within slabs brings the already-known advantages of conventional flat slab systems with the weight reduction caused by removing concrete from less stressed structure regions. However, it is necessary to carefully assess the punching shear phenomenon, mainly when unbalanced loads are applied. Thus, a numerical simulation using the Finite Element Method was developed, and validated with experimental data from four slabs, one solid, and three slabs with spherical voids. The results demonstrated good approximations when unbalanced loads were considered for load-displacement behavior, load-strain in concrete and reinforcements, and failure surface. Overall, a decrease in ultimate load, stiffness, and load at the first crack was identified when spherical voids were used.

Keywords: flat slabs with voids, finite element method, punching shear, ANSYS, reinforced concrete structures.

Resumo: O emprego de vazios esféricos no interior das lajes agrega as vantagens já conhecidas do sistema de lajes lisas convencionais com a redução de peso provocada pela retirada de concreto de regiões pouco solicitadas da estrutura. Todavia, é necessário avaliar com maior cautela o fenômeno da punção, especialmente quando são aplicadas cargas desbalanceadas. Assim, foi desenvolvida uma simulação numérica pelo Método dos Elementos Finitos, validada com dados experimentais de quatro lajes, sendo uma maciça e três lajes com vazios esféricos. Os resultados demonstram boas aproximações quando as cargas desbalanceadas foram levadas em consideração, tanto para o comportamento carga-deslocamento, carga-deformação no concreto e nas armaduras e superfície de falha. De forma geral, foi possível identificar queda na carga de ruptura, na rigidez e na carga da primeira fissura quando foram empregados vazios esféricos.

Palavras-chave: lajes lisas com vazios, método dos elementos finitos, punção, ANSYS, estruturas de concreto armado.

How to cite: E. R. Z. Schimanowski, A. Campos Filho, B. M. Lazzari, and P. M. Lazzari, "Numerical simulation of punching shear in flat slabs with spherical voids subjected to symmetric and asymmetric loadings," *Rev. IBRACON Estrut. Mater.*, vol. 17, no. 3, e17316, 2024, https://doi.org/10.1590/S1983-41952024000300016

Corresponding author: Eric Renã Zavitzki Schimanowski. E-mail: ezschimanowski@gmail.com
Financial support: This study was fully financed by the Civil Engineering Graduate Program (PPGEC) of the Federal University of Rio Grande do Sul (UFRGS) and by the Brazilian governmental research institutions CAPES and CNPQ.
Conflict of interest: Nothing to declare.
Data Availability: The data that support the findings of this study are available from the corresponding author, E. R. Z. Schimanowski, upon reasonable request.

1 INTRODUCTION

The flat slab system is known for presenting interesting advantages in the construction industry, such as savings in formwork and concrete, simplification in complementary projects, easier and faster execution, improved ventilation and lighting, and greater architectural freedom [1]. However, despite the ease of formwork execution and assembly due to the absence of beams, the high self-weight of this system makes it economically impractical for use in large spans, tall buildings, and seismic-prone regions [2]. To overcome large spans, for instance, it becomes necessary to increase the thickness of the slab due to the transfer of vertical loads, impacting not only material consumption but also the loads acting on the foundations.

To solve this problem, it is possible to replace the region of concrete subjected to low stresses with hollow plastic voids [3]–[5]. In this system, the voids are typically conformed by high-density polyethylene (HDPE) and remain inside the slab after concreting, secured by steel meshes, and positioned between two layers of reinforced concrete (Figure 1). When voids of spherical shape are employed, Schnellenbach-Held and Pfeffer [6] point out that the reduction in self-weight can reach up to 30%.

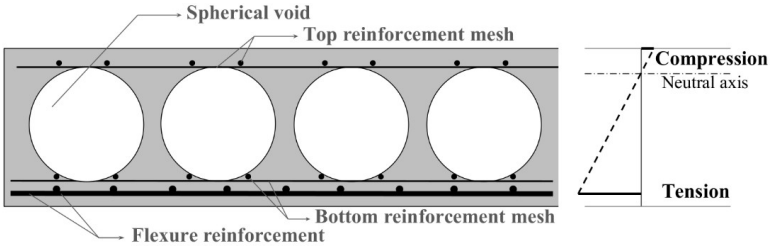

Figure 1. Flat slab section with spherical voids.

Although the spherical shape is the most common, the literature points to the existence of other geometries, such as cuboids, ellipsoids, donut formats, and mushrooms, among others [2]–[9]. For any shape, using voids changes the slabs' behavior. In most studies, flat slabs with voids exhibit less rigid load-displacement response [5], [10]–[12], reduction in the first crack load [13]–[15], and lower flexural [3], [12], [15] and shear [13], [16] failure loads compared to solid slabs.

Furthermore, due to the absence of beams, the flat slab system with voids requires special attention regarding punching shear. As presented by Silva et al. [1], this phenomenon occurs due to the concentration of shear stresses in the region near the slab-column interface, forming a punching shear cone. Since it is a more fragile rupture, punching occurs abruptly, without prior warning, and can lead to partial or total collapse of slabs, even resulting in the complete failure of the structure in extreme cases.

Various parameters impact this phenomenon with different degrees of intensity, such as slab thickness, concrete properties, flexural reinforcement ratio, shape and dimensions of the column, and the presence of shear reinforcement [17]–[19]. In the case of flat slabs with voids, some additional factors must also be taken into account, such as the shape and dimensions of the voids, horizontal spacing, concrete cover, material of the voids, and, especially, the solid region around the column [4]–[8], [10].

In the punching shear of flat slabs with voids, Chung et al. [10] point out that the failure load varies according to the position of the voids and becomes higher when the distance between the first layer of voids and the face of the column increases. The authors found that, for the case of voids in the donut shape, for example, the model depicted in Figure 2a exhibited a punching load of 641.5 kN, a value 15% lower than that obtained by the model shown in Figure 2b, where the voids are further away from the column.

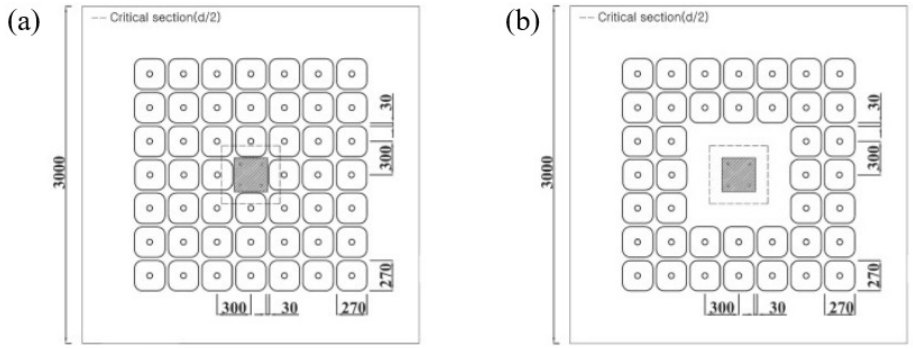

Figure 2. Variation in the position of the voids (dimensions in mm) [10].

This conclusion has also been verified in different studies, with a consensus that the solid region has a direct impact on the structure's behavior [4], [6], [8], [10], [20]. When this region is small, punching shear is more critical, and the failure load is significantly lower than in solid slabs. On the other hand, when the voids are sufficiently far from the column, the punching shear cone does not intersect them, and the structure's behavior is similar to conventional flat slabs.

However, another parameter that also impacts punching is the asymmetry of loads, a parameter little studied in flat slabs and even less studied in flat slabs with voids. Ferreira et al. [21] mention that, in structural design practice, for solid flat slabs, punching is always eccentric due to the asymmetry of spans and loads. The same authors also indicate that load asymmetry reduces punching resistance, making this failure even more critical.

In this context, the present study aims to analyze the performance of slabs with spherical voids subjected to symmetric and asymmetric punching failures. To achieve this objective, a numerical model was developed using the Finite Element Method (FEM) through the ANSYS software. Initially, the model was validated using experimental data obtained by Lima [22] and Nicácio [23], which encompass four types of slabs, one of them being solid and the other three containing spherical voids, which unintentionally presented load asymmetry during the tests. Nicácio [23] points out that this asymmetry in loadings occurred due to an error in a digital indicator in one of the load application cells, resulting in an unbalanced loading due to the greater load application in one direction. Thus, through the numerical model, this study seeks to evaluate the behavior of the mentioned slabs under symmetric loading, comparing it with asymmetric punching, and also discuss the impact of each type of loading on different results, such as displacements, failure loads, and deformations in concrete and reinforcement.

2 MATERIAL CONSTITUTIVE MODELS

For concrete modeling, the constitutive models implemented by Lazzari et al. [24], [25], Hoffman et al. [26], Machado et al. [27], and Soares et al. [28] were used in a customized routine on the ANSYS software. For compression, an elastoplastic model with hardening was adopted, which includes a failure criterion, a plastification criterion, and a hardening rule. The failure surface of Ottosen [29] was used as recommended by the *fib* Model Code 2010 [30].

Regarding plastification, it was considered that the concrete exhibits isotropic hardening and a plastification surface with the same shape as the failure surface, describing uniform expansion in the deviatoric plane. For the hardening rule, which defines the movement of the loading surfaces, the relationship between stress and effective plastic strain corresponds to the concrete's behavior under uniaxial tests. Thus, the stress vs. strain diagram under uniaxial compression proposed in the *fib* Model Code 2010 [30] was used.

For concrete under tension, a linear elastic behavior until failure was considered, and after cracking, softening was incorporated, as suggested by Cervera et al. [31]. The distributed model with the fixed crack solution was used for crack modeling, where the finite element mesh has no separation and remains continuous. Thus, the properties of the concrete are modified, and only the stress-strain relationship is updated. The model for concrete under tension consists of a cracking criterion, a tension stiffening rule, and a model for transferring shear stresses.

As proposed by CEB Bulletin nº 156 [32], in the cracking criterion, if the principal stress is greater than half of the tensile strength, the integration point cracks; otherwise, it crushes. Thus, the stiffness in each direction was considered separately, and the stress vs. strain diagrams corresponding to uniaxial forces were used for each of the two principal directions in the cracking plane. In the model for transferring shear stresses, a parameter was adopted to reduce the transverse modulus of elasticity, allowing the direct incorporation of this behavior into the distributed cracking model.

In the rule for contribution between cracks, tension stiffening was considered by assuming a perfect bond between reinforcement and concrete. Thus, the damage was defined through the descending branch of the concrete's stress vs. strain diagram under uniaxial tension.

Concerning the reinforcements, it was considered that they resist only axial forces. Thus, a uniaxial elastoplastic model was adopted. Due to the characteristics of the steel determined through experimental tests, perfect plasticity without hardening was assumed. In this scenario, the stress vs. strain diagram exhibits linear elastic behavior until the yield stress is reached and then remains constant.

To model the time-dependent behavior of concrete, phenomena such as creep and shrinkage were also considered, taking into account experimental results of material properties and estimates for environmental parameters. The formulations were based on the CEB-FIP Model Code 1990 [33] and implemented as presented by Quevedo et al. [34].

3 COMPUTATIONAL MODEL

The FEM is widely employed for computational analyses of reinforced concrete structures because it allows the consideration of material nonlinearity. Thus, it analyzes a physical problem through complex mathematical models that

consider the discretization of a continuous domain into a finite number of elements, typically using computational programs [35].

For this study, the slabs were analyzed in ANSYS 21.2 using APDL (ANSYS Parametric Design Language) input scripts. These scripts contained geometry data, material properties, loads, element types, and other relevant information.

The concrete was modeled using the SOLID186 element with a tetrahedral shape, available in the ANSYS library [36]. This element consists of 10 nodes, with three degrees of freedom each, allowing translations in the three directions (X, Y, and Z). Due to its number of nodes and quadratic interpolation, the element can be used in less refined meshes. It was chosen for its compatibility with USERMAT and the reinforcement elements adopted for the reinforcement bars. Furthermore, the tetrahedral shape was chosen to model the spherical voids adequately.

The BISO (Bilinear Isotropic Hardening) model available in the ANSYS library was adopted for the steel modeling, considering the steel reinforcement bars as reinforcement elements. The embedded model was used for the reinforcement, so the concrete and steel nodes do not need to coincide. The REINF264 element was used to implement the steel, which has local coordinates, degrees of freedom, and connectivity identical to the base elements used in the concrete. MESH200 mesh elements were also used.

The constitutive models of the concrete were incorporated into ANSYS using the UserProgrammableFeatures (UPF) tool in a routine called USERMAT. Various studies from the Civil Engineering Post Graduate Program at the Federal University of Rio Grande do Sul (PPGEC/UFRGS) developed and updated this routine over the years.

4 STRUCTURAL CHARACTERISTICS

Lima [22] and Nicácio [23] developed an experimental program composed of four slabs, as shown in Figure 3: one solid slab (RSP28), serving as a reference specimen and three slabs with spherical voids (BD28-P1, BD28-P2, and BD28-P3). All the slab prototypes have dimensions of 2,500 × 2,500 × 280 mm. In the center of each slab, there is a circular reinforced concrete column with a diameter of 300 mm, extending 800 mm above and 400 mm below the slab surface. For the slabs with voids, Recycled Plastic Hollow Spheres (RPHS) made of high-density polyethylene, with a diameter of 225 mm and spaced at 250 mm in both directions on the slab, were used. In slabs BD28-P2 and BD28-P3, four precast floor plates with a thickness of 50 mm were used, as indicated by the lines shown in Figure 3. To connect the precast floor plates, 10 mm linking bars were employed.

For the flexural reinforcement, 20 bars of steel CA50 with a 12.5 mm diameter were used in each direction, positioned on the top surface with a concrete cover of 25 mm, which was subjected to tension (Figure 4). In the slabs with voids, the RPHS are held in place by using a top and bottom steel mesh with 6 mm and 8 mm diameter bars, respectively. This reinforcement scheme is also applied to the reference slab to ensure consistent flexural reinforcement across all slabs in the experimental program.

For the BD28-P2 and BD28-P3 slabs, CA50 steel bars with a diameter of 10 mm and spaced at 250 mm were placed to the joints of the precast concrete layers. In slabs with voids, steel girders were used to secure the voids between the top and bottom reinforcement and facilitate the lifting and transportation of the precast floor plates. Figure 5 displays all the reinforcements used in the BD28-P2 model, for example, as well as the spheres and the precast floor plate.

In the BD28-P3 model, closed stirrups made of CA50 steel were used for the punching shear reinforcement, arranged in a single direction, produced with 6.3 mm diameter bars, and fixed to longitudinal bars with a diameter of 8 mm, as shown in Figure 6.

Regarding the material properties, Table 1 presents data related to concrete, such as compressive strength and tensile strength obtained, respectively, through uniaxial compression and tensile by diametrical compression tests on 100 × 200 mm cylindrical specimens. Additionally, the same table also provides experimental data for the steel, including the modulus of elasticity and yield stress for each gauge used.

In the execution of the slabs, the casting of the precast floor was initially performed for the BD28-P2 and BD28-P3 models. After 58 days, the additional concrete was added, and the remaining slabs were executed. After 44 days of final concreting, the experimental tests were performed. Thus, when the slabs were tested, the concrete age of the precast floor was 102 days.

To simulate punching shear, the conducted test involved fixing the column and applying loads at eight different points through hydraulic actuators, as shown in Figure 7a. The load was applied to each metal beam, redistributed to two steel plates, and thus applied to the slab. Figure 7b illustrates the positions of the load application plates. Additionally, Figure 8a depicts a slab in the testing system, and Figures 8b and 8c show the column fixation in the testing system on the upper and lower faces, respectively.

Figure 9a shows the positions of the 12 linear variable-displacement transducers (LVDTs), located on the upper surface of the slab, used to obtain the results. It is worth mentioning that some reading points were arranged equidistant from the center of the slab, in symmetrical positions, such as LVDTs L1, L6, L7, and L12, for example.

As for the concrete deformations, the results were obtained using strain gauges positioned on the underside of the slab, near the column, as shown in Figure 9b. Additionally, the positions of the strain gauges used to determine deformations in the flexural reinforcement (Figure 9c) and punching shear reinforcement (Figure 9d) are also presented.

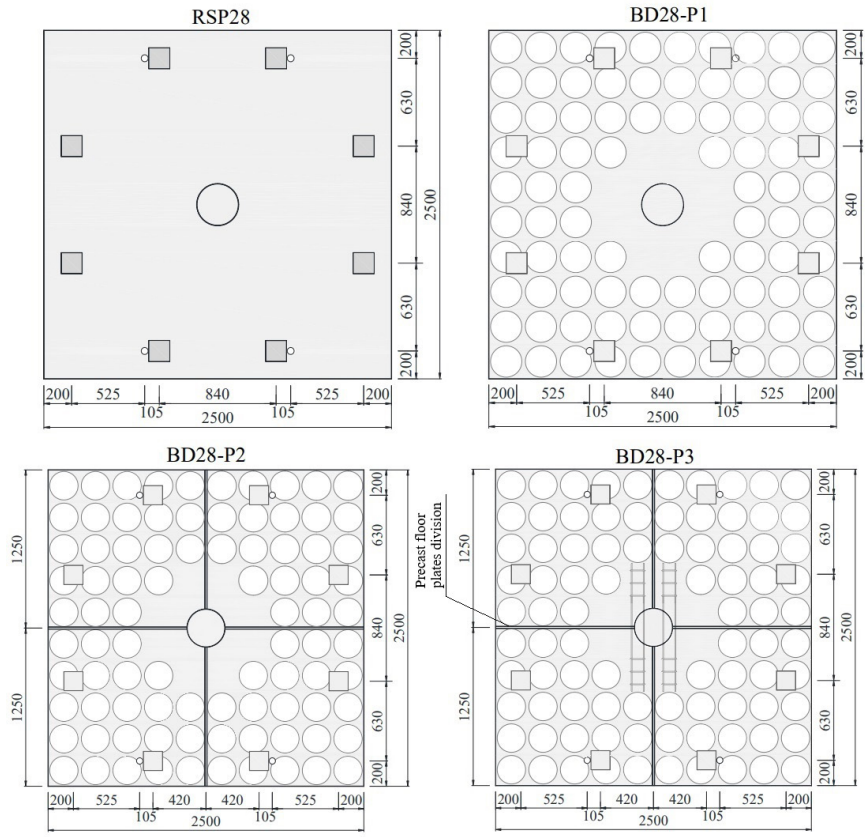

Figure 3. Characteristics of tested slabs (dimensions in mm) [23].

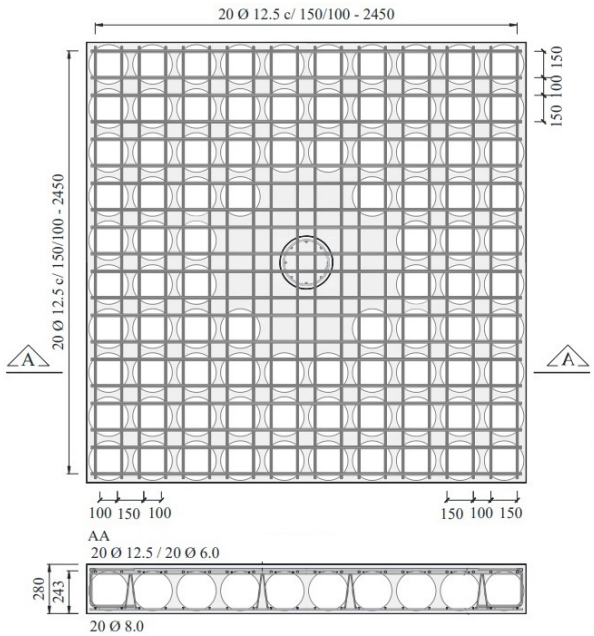

Figure 4. Configuration and details of flexural reinforcement (dimensions in mm) [23].

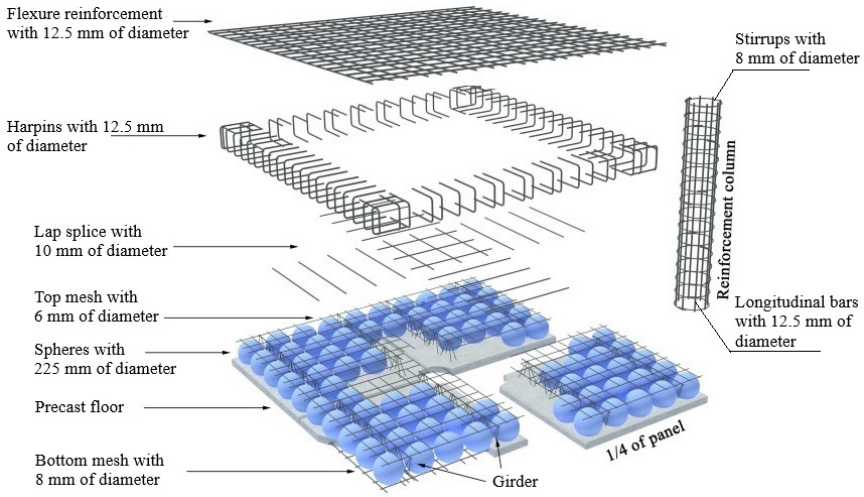

Figure 5. Reinforcement configuration [adapted from Nicácio [23]].

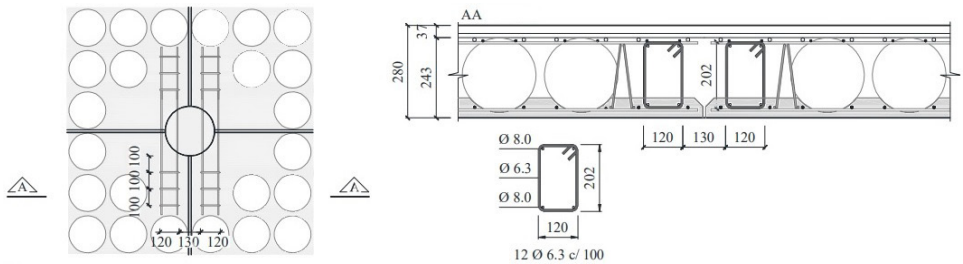

Figure 6. Configuration of punching shear reinforcement (dimensions in mm) [23].

Table 1. Material properties.

Material	Specification	Compressive strength (MPa)	Tension strength (MPa)	Yielding stress (MPa)	Modulus of elasticity (GPa)
Concrete	Slab	48	3.8	-	36
	Precast floor	57	3.5	-	38
Steel	φ = 6 mm	-	-	697	195
	φ = 6.3 mm	-	-	622	198
	φ = 8 mm	-	-	558	195
	φ = 8 mm (mesh)	-	-	644	195
	φ = 10 mm	-	-	553	193
	φ = 12.5 mm	-	-	584	189

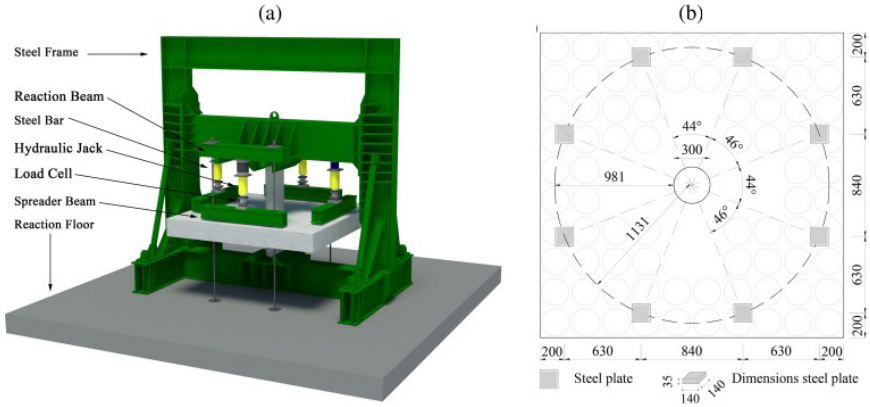

Figure 7. (a) Test setup and (b) location of the load was applied (dimensions in mm) [23].

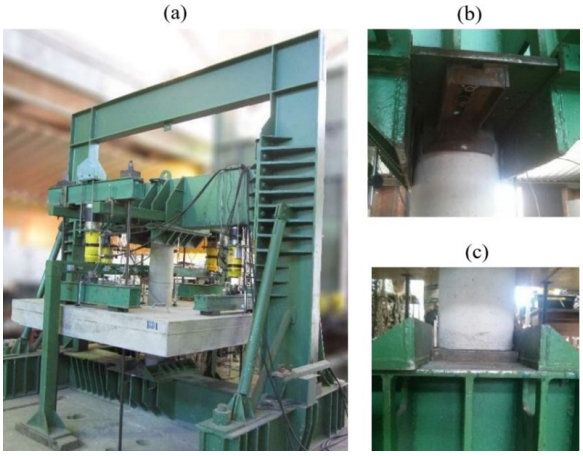

Figure 8. (a) Experimental test, (b) top and (c) bottom column support [22], [23].

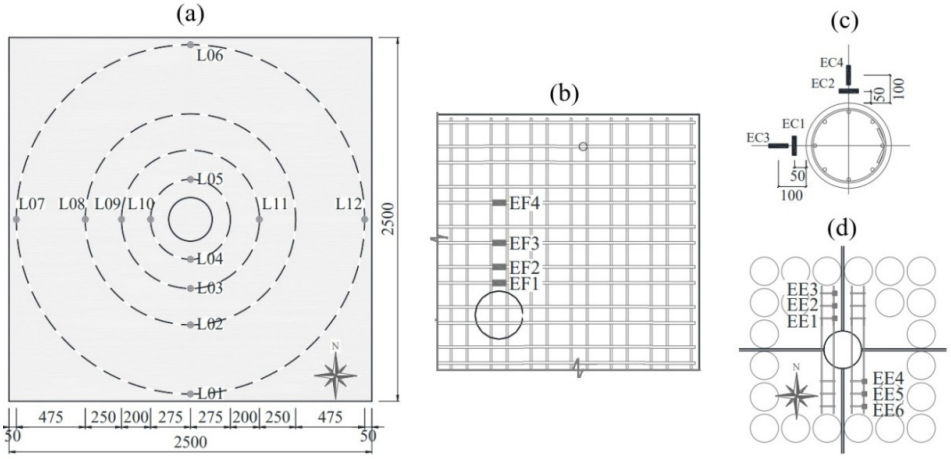

Figure 9. Arrangement of (a) linear variable-displacement transducers, (b) strain gauges on the flexural reinforcement, (c) strain gauges on the slab's bottom concrete surface, and (d) strain gauges on stirrups (dimensions in mm) [23].

5 NUMERICAL MODEL

Due to the symmetry of the experimental models, only a portion of the slab was modeled, as shown in Figure 10. Therefore, displacement constraints were imposed on the symmetry faces. This measure reduced processing time, as fewer elements were used in the modeling. Therefore, after creating the concrete volume of the slab, spherical volumes were removed for void modeling using available boolean commands in the software. For the column, volume extrusion commands were used, employing concrete with the same characteristics as the slab.

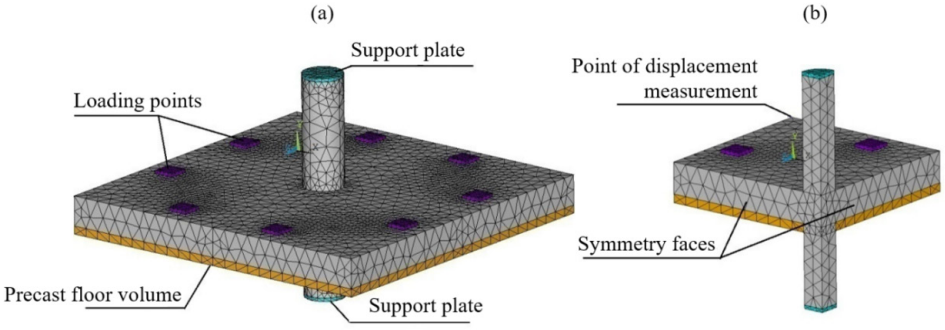

Figure 10. (a) Support and loading application condition and (b) modeling of one-quarter of the slab due to symmetry.

The load application and support plates were modeled as high-rigidity materials, following the positions and conditions of the test procedure. As for the precast floor, the initially created concrete volume was divided into two, allowing each new volume to be modeled with distinct ages and properties.

Regarding the steel bars, Figure 11 presents the modeling of the flexural reinforcement and its anchorage according to experimental data. The other reinforcements, such as top and bottom meshes, trusses, anchoring bars of the precast floor, and punching shear reinforcement, were also modeled according to the experimental program. In the column, a greater number of longitudinal bars were employed to better organize the reinforcement distribution over the modeled concrete volume, maintaining the same reinforcement ratio over the section area and the same quantity of stirrups. This measure was taken to avoid the accumulation of stresses in elements arranged near the symmetry faces.

Moreover, regarding the concrete properties, experimental values were used for tensile and compressive strength. Other properties were calculated within the USERMAT, such as modulus of elasticity and factors that take into account the strength gain over time, for example. For calculating these properties, USERMAT utilizes formulations presented in the CEB-FIP Model Code 1990 [33].

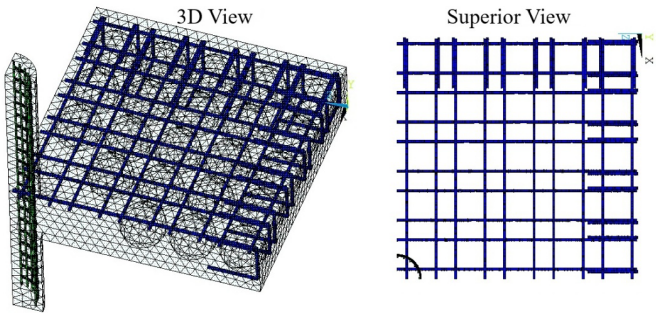

Figure 11. Modeling of the flexural reinforcement.

Additionally, other parameters were inserted into the input scripts, such as curing time of 7 days, ambient temperature of 25°C, and Poisson's ratio of 0.2. Since the location where the slabs were executed has low relative humidity, it was considered an important factor to be modeled. In this regard, as the formwork remained in the slabs until the loading age, water release from the concrete occurred mainly through the upper face of the slab.

To consider this behavior, the concrete volume was divided into two, creating a region near the upper face with a constant thickness of 5 cm, where a critical value for humidity, equal to 40%, was considered. A higher humidity of 80% was adopted for the remaining sections of the slab. This measure did not significantly alter the structure's behavior regarding displacements but provided a better approximation of the load at the first crack.

Thus, time increments were used to take into account the time-dependent behavior of concrete and simulate real conditions, which include the effects of creep and shrinkage. Two loading steps were applied that consisted of the passage of time, one with a 7-day increment corresponding to the drying age and another from 7 days until one day before the test. In the case of the existence of a precast floor, its age was considered in the model through a USERMAT variable called “texist,” which takes into account the age before the solution process begins in the software.

After the passage of time, the self-weight of the structure was applied one day before the test date. Then, the 4th load case was applied in an increment of 0.1 days, fixing the displacements to start the test simulation. This step is essential for the software to consider deformations related to shrinkage.

To evaluate the behavior of the structure under the imposed loading, displacement increments were applied to the central node of the modeled plates, characterizing the 5th and final load case. In the software, the displacement increments were considered equal and distributed over one day.

The plotting of curves and experimental results refers only to the 5th loading step, which consists of the test simulation. Due to this, the displacement obtained in the modeling for the first increment of this loading step was reset to create the initial point of the graph with self-weight on the ordinate axis and initial displacement equal to zero on the abscissa axis.

Furthermore, preliminary tests were conducted to determine the best configuration, considering the model's behavior for different meshes. Different maximum dimensions for the elements were adopted, ranging from 7.5 to 15 cm. Given this situation, the maximum element dimension that showed results closest to the experimental data, 10 cm, was adopted.

6 RESULT ANALYSIS

Due to the asymmetric and variable loading for each slab, the experimental data presented by Lima [22] and Nicácio [23] do not allow for a direct comparison between the studied slabs. Therefore, it would not be possible to conclude how the presence of spheres, precast floors, and the shear reinforcement interferes with the structure's behavior in the experimental analysis.

From this perspective, the initial numerical modeling took into account the asymmetric loading imposed on the structure in the experimental test based on the verification of displacements at each LVDT, as described in 6.1, to enable the utilization of experimental data and validate the numerical model. In this modeling, the peculiarities of each model were considered, which are discussed and presented in detail in the following sections.

Furthermore, equal displacements were used for all slabs' application points, configuring a symmetric loading. With this data, it was possible not only to analyze the slabs directly but, more importantly, to assess the impact of asymmetric punching shear on the rupture load, load-displacement, load-deformation, and failure surface.

6.1 Load versus displacement

In the loading steps, as it was considered that the formwork used in the concreting was removed only one day before the test, the slab was not subjected to any applied load until that age. However, as low humidity was considered on the upper face, the phenomena of shrinkage and creep generated displacements in the structure in the opposite direction to the application of load. In the real case, the test starts from this configuration, so in ANSYS the applied loading was also imposed on these initial displacements, which were subtracted for plotting curves and data analysis.

Regarding the load application, it was observed that the unbalanced in the load application system caused asymmetric displacements, as can be identified in Figure 12 for the BD28-P2 slab, for example. Since the unbalanced loadings were not an objective of the experimental study, no data on the load application at each point are provided. Nevertheless, displacements were provided from LVDTs 1, 6, 7, and 12, which were positioned near the load application points. In this context, it was possible to model asymmetric punching by considering the proportion between the displacements of the structure at different positions obtained in the experimental test. Thus, the load in the numerical model was applied following this proportion.

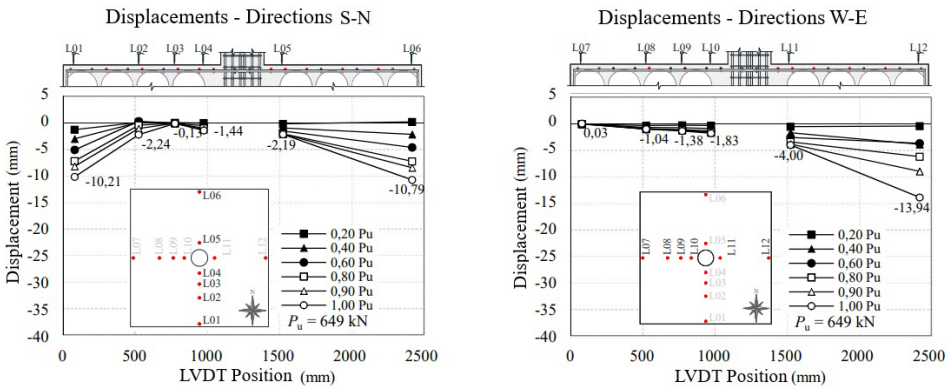

Figure 12. Displacements of BD28-P2 slab [23].

The BD28-P1 and BD28-P3 slabs showed similar displacements for each pair of LVDTs, meaning that out of the 4 points of measurement farthest from the column, 2 showed larger displacements, close to each other, and the other 2 points showed smaller displacements, also close to each other. Taking this into account, the proportion applied in the numerical model of a quarter of the BD28-P1 slab was set to 0.25, indicating that when applying an imposed displacement of 1 cm on one plate, only 0.25 cm was applied to the other plate. This measure brought the numerical curves closer to the experimental data at different points on the slab, as shown in Figures 13, 14, 15, and 16

In this sense, it can be seen that the numerical model is capable of simulating punching failure for unbalanced loadings with good approximation in the load at the first crack and rupture load. Additionally, the numerical model remained stiffer than the experimental data, at least in one of the curves presented at each measurement point. In the points farthest from the column, shown in Figure 13, the asymmetric loading showed good approximation. In the intermediate points, the model was not as precise, as only two LVDTs were used to collect displacements, making it impossible to assess the behavior in other directions.

In symmetric loading, the two curves obtained for the modeled quarter of the slab overlap. Thus, it can be observed that the numerical curve reaches significantly higher rupture loads, as well as cracking loads and higher stiffness when compared to asymmetric loading, deviating from the experimental data at all measurement points.

In the BD28-P3 model, the same procedure was considered, with the proportion between the imposed displacements equal to 0.3, which also better approximated the cracking load, stiffness, and rupture load when compared to the results of symmetric punching. Figure 17 shows the load-displacement curve for the point farthest from the column, which includes LVDTs 1, 6, 7, and 12, for the asymmetric loading case (Figure 17a) and symmetric loading (Figure 17b).

For the RSP28 slab, which showed greater variability in the data, the results of the LVDTs with the largest and smallest displacements were compared. Thus, a proportion of approximately 0.3 was verified. The impact on the slab displacements and rupture load could be observed in Figure 18 when applying asymmetric and symmetric loading. In the load-displacement curves, a closer approximation can also be observed when considering unbalanced loadings, especially regarding the rupture load, as shown in Figure 19.

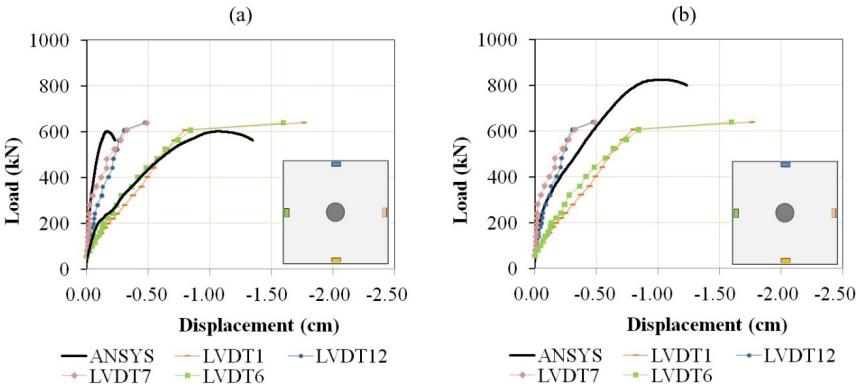

Figure 13. Load-displacement curve for LVDTs 1, 6, 7, and 12 of the BD28-P1 slab for (a) asymmetric loading and (b) symmetric loading.

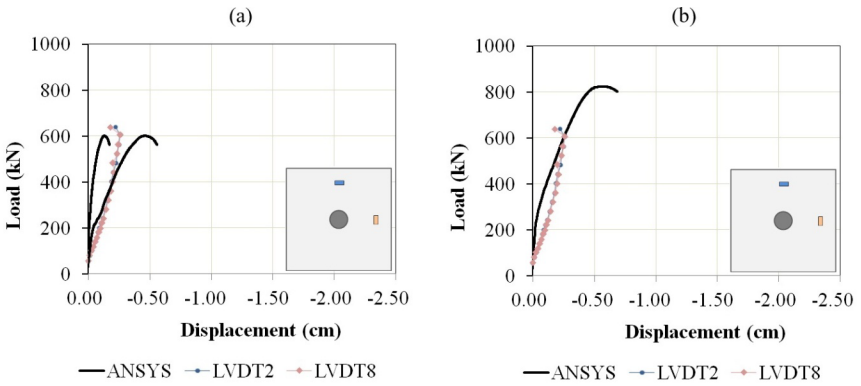

Figure 14. Load-displacement curve for LVDTs 2 and 8 of the BD28-P1 slab for (a) asymmetric loading and (b) symmetric loading.

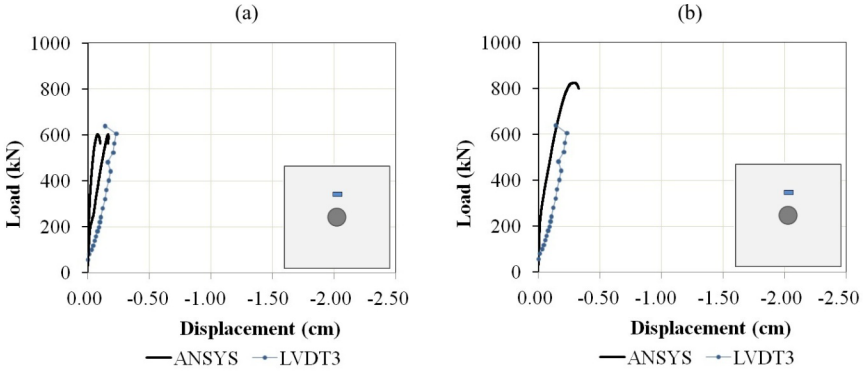

Figure 15. Load-displacement curve for LVDT 3 of the BD28-P1 slab for (a) asymmetric loading and (b) symmetric loading.

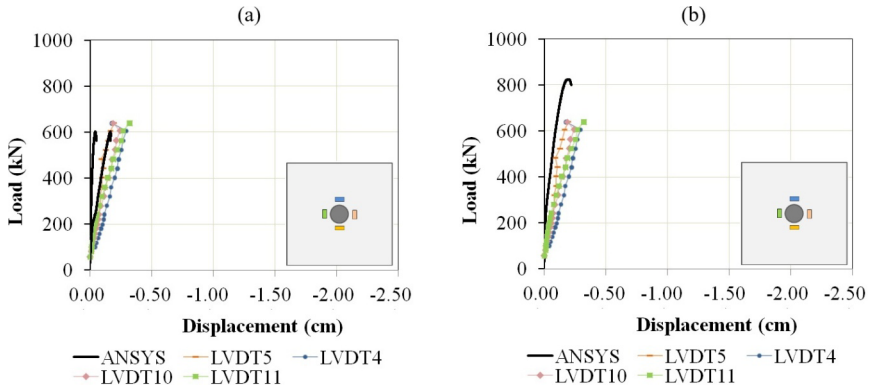

Figure 16. Load-displacement curve for LVDTs 4, 5, 10, and 11 of the BD28-P1 slab for (a) asymmetric loading and (b) symmetric loading.

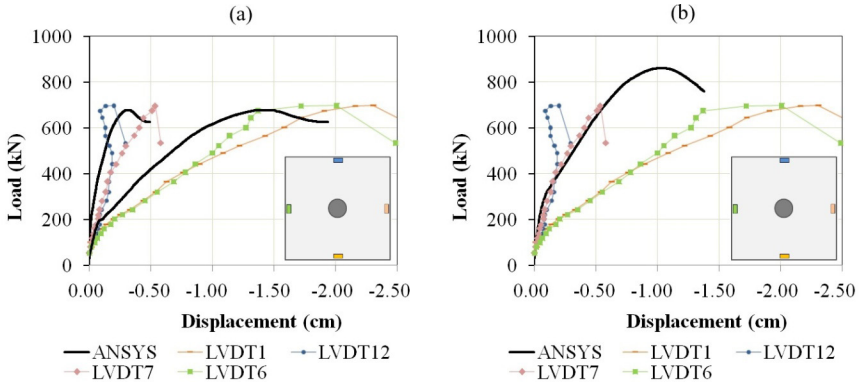

Figure 17. Load-displacement curve for LVDTs 1, 6, 7, and 12 of the BD28-P3 slab for (a) asymmetric loading and (b) symmetric loading.

As for the BD28-P2 slab, it was necessary to assess the behavior differently, as one of the LVDTs remained null for most of the test, showing positive displacement at the rupture load. Thus, as shown in Figure 20a, it was necessary to model 1/2 of the slab, not only 1/4 as in all other models. Symmetry commands were used in the input script during the mesh generation. Consequently, to replicate the experimental behavior, a zero-prescribed displacement (dy=0) was applied to one of the plates, and equal displacement increments were imposed on the other plates. From this, the displacement behavior can be observed in Figure 20b, which indicates the lack of symmetry.

For this slab, the data varies differently, as the displacement of LVDT 6 increases and then decreases, indicating that the applied load changed significantly during the test. This behavior was not considered in the modeling, and greater discrepancies between experimental and numerical results were expected, but still, an approximation to symmetric loading, as shown in Figure 21.

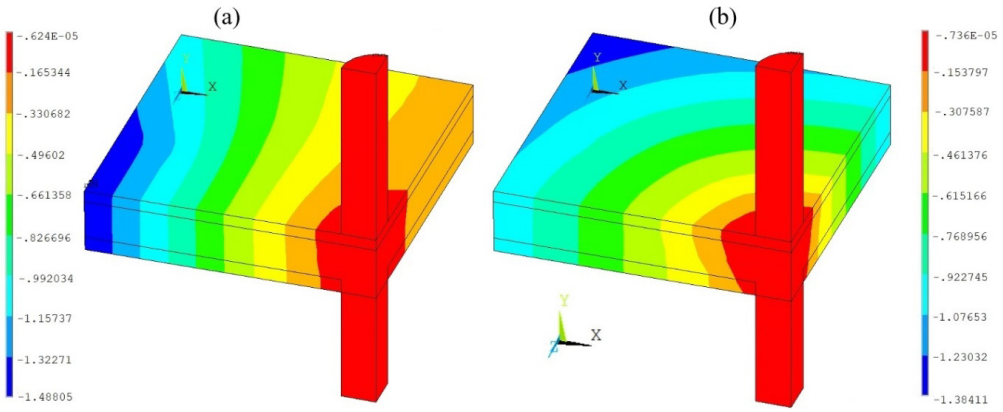

Figure 18. Displacements at rupture load of the RSP28 slab for loading (a) asymmetric and (b) symmetric1.

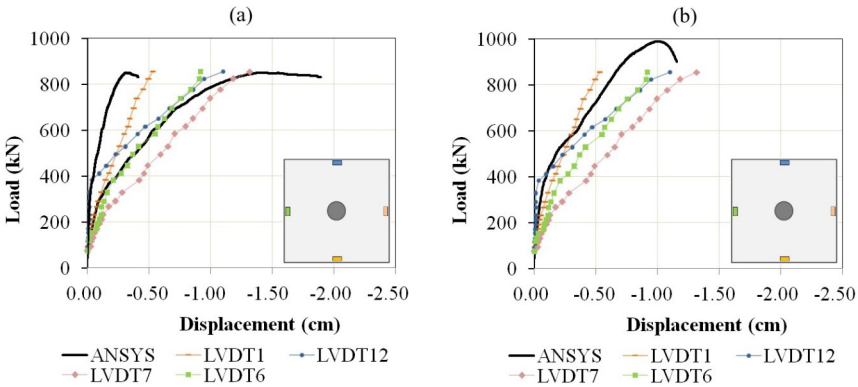

Figure 19. Load-displacement curve for LVDTs 1, 6, 7, and 12 of the RSP28 slab for (a) asymmetric loading and (b) symmetric loading.

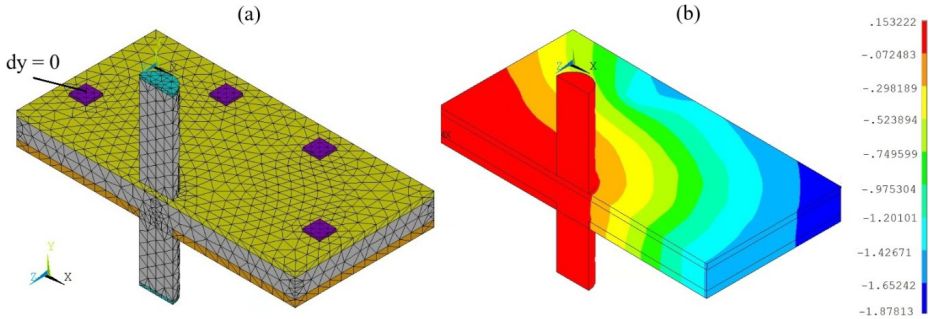

Figure 20. (a) Numerical model of the BD28-P2 slab and (b) displacements at rupture load.

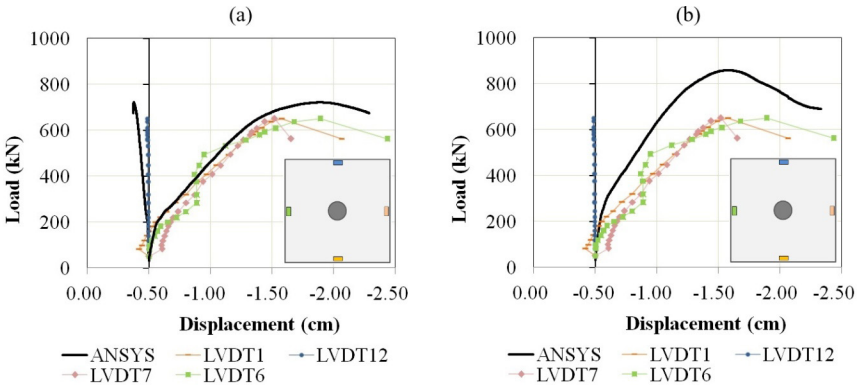

Figure 21. Load-displacement curve for LVDTs 1, 6, 7, and 12 of the BD28-P2 slab for (a) asymmetric loading and (b) symmetric loading.

Therefore, it is clear that the asymmetric loading approach provides results closer to the experimental data for all analyzed models, even with the peculiarities of each slab and the approximations made in the modeling. By considering asymmetric punching shear, the numerical model showed an approximation of the load relative to the first crack, stiffness, and rupture load.

In this way, considering that the experimental data were adequately validated for the asymmetric case, it is possible to use the results obtained under symmetric loading to compare the models directly. Thus, it is observed that the solid slab model (RSP28) showed a load relative to the first concrete crack close to 400 kN, a value higher than that obtained for the voided slabs (BD28-P1, BD28-P2, and BD28-P3), 250-350 kN, due to the removal of concrete spherical volumes, which reduces the portion of concrete resisting tension. Additionally, it is also possible to identify higher stiffness in the solid slab, due to the greater moment of inertia, and a higher ultimate load, as the voids intercept the punching shear cone.

6.2 Punching shear capacity

The rupture loads obtained consider the slab's self-weight and the load applied by the testing system, as shown in Table 2. When adopting asymmetric loading, the difference found in the modeling was small, highlighting the solid

slab RSP28 that presented a load only 0.5% lower than the experimental one. On the other hand, if symmetric loading were considered, the rupture load obtained in the modeling would be 15.64% higher than the experimental data.

Directly comparing the solid slab model (RSP28) with the one with voids (BD28-P1) through loads obtained for symmetric loading, it can be observed that there was a 16.63% reduction for the second model. This difference indicates that the presence of voids interferes with the behavior of the structure subjected to punching shear. This can be explained because the punching cone forms under the spheres, reducing the resistant concrete region. Additionally, the modeling also allowed verifying the reduction in the self-weight of the structure, which reached approximately 28% when voids were employed in the analyzed models.

Table 2. Punching shear capacity of experimental data and numerical simulation.

Slab	Experimental punching shear capacity (kN)	Type of loading	Punching shear capacity of numerical simulation (kN)	Difference (%)
RSP28	855	Asymmetric	850,70	-0.50
		Symmetric	988.74	+15.64
BD28-P1	639	Asymmetric	601.53	-5.86
		Symmetric	824.27	+28.99
BD28-P2	649	Asymmetric	720.97	+11.26
		Symmetric	857.89	+32.39
BD28-P3	693	Asymmetric	677.75	-2.20
		Symmetric	860.88	+24.23

Regarding the BD28-P2 model, although considering unbalanced loading favored an approximation to the experimental data, reducing the difference from 32.39% to 11.26%, it was found that the modeling still overestimates the rupture load. Specifically for this slab, this behavior can be explained by the variation in the load applied at a specific point during the test, which was not taken into account in the modeling, as discussed earlier.

Comparing the slabs BD28-P1 and BD28-P2, which differ only in the presence of a precast floor in the second model, it can be seen that there was a small increase in the load resistance (4%) for symmetric loading. This behavior is explained by the higher compressive and tensile strength of the precast floor, which is greater than in the concrete complement. However, as the thickness of the precast floor is small, the impact on the final behavior of the slab is not very evident.

Analyzing the BD28-P2 and BD28-P3 models, which differ in the use of shear reinforcement in the second slab, it was possible to verify that this choice of reinforcement did not have a significant impact, as it did not increase the rupture load in symmetric loading. This behavior is associated with the use of reinforcement in one direction, which does not prevent the formation of the punching cone in other directions and, therefore, does not significantly interfere with punching shear, for the presented case.

6.3 Concrete strains

Concrete strains were collected for all analyzed models, both in the radial and tangential directions, in the region subjected to compressive forces. In all cases, considering asymmetric loading provided a better approximation of simulation results to experimental data, especially for data near the rupture load. Thus, Figure 22 presents the strains for the BD28-P3 model, subjected to asymmetric loading.

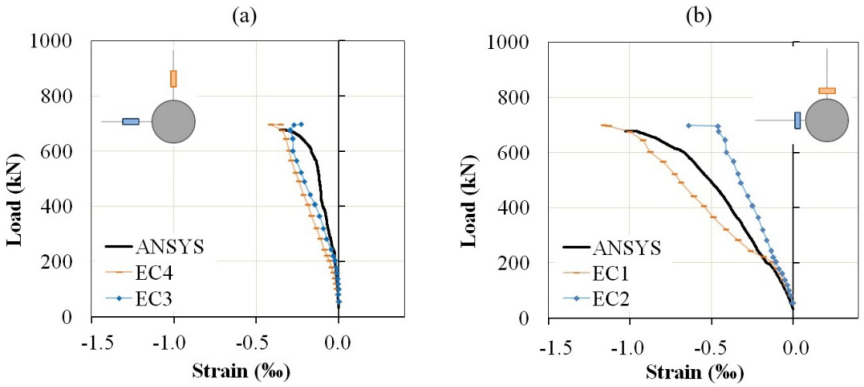

Figure 22. Concrete (a) radial and (b) tangential strains of BD28-P3 slab.

The results indicate that the numerical model can reproduce the experimental data with good approximation. Similar behaviors were also observed in the other models, with all slabs showing maximum strains lower than the concrete crushing strain, typical of punching shear failure.

6.4 Strains in the flexural reinforcement

As depicted in Figure 23, for the BD28-P2 model, the strain of the reinforcements obtained for all slabs, at all measuring points, was close to the experimental data when the asymmetry loading was taken into account. Good agreement can be observed concerning the first crack load, at which point the steel starts to exhibit higher strains. A good agreement can also be observed in strain corresponding to failure load.

When considering symmetric loading, there was a greater difference in the curves, especially concerning the first crack load, which was higher for these cases. The rate of strain variation was similar for both loadings cases since the steel's properties were not altered, resulting in similar curve inclination after the first crack load in concrete.

Moreover, it is also possible to observe that only in the first two measuring points did the bars reach the yield stress and begin to exhibit high strains. This behavior further supports the conclusion that the numerical model is failing due to punching shear, as the experimental slabs. Similar behaviors were observed in all models, with only a few reinforcement elements reaching the yield stress.

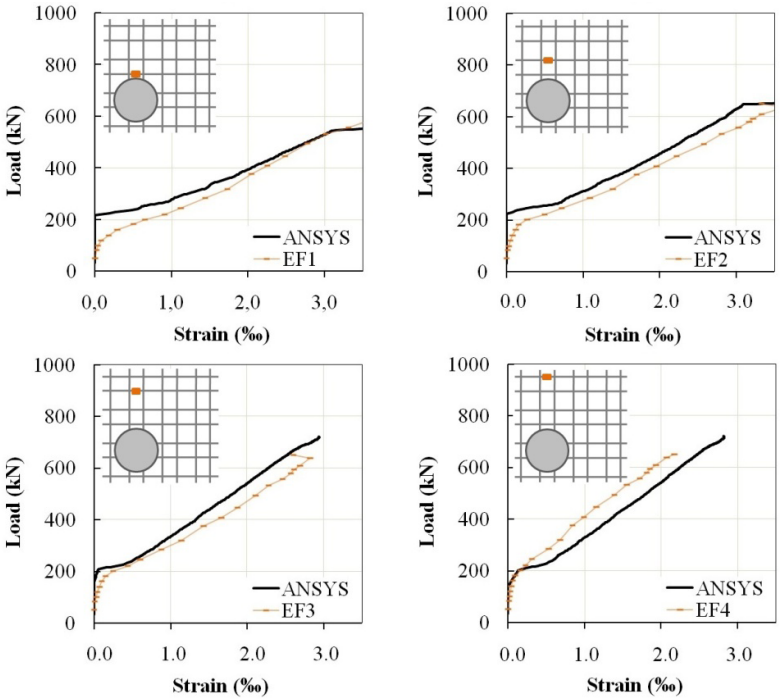

Figure 23. Axial strains in flexural reinforcement of BD28-P2 slab.

6.5 Strains in the punching shear reinforcement

Regarding shear reinforcement, only present in the BD28-P3 slab, it was observed that the strain corresponding to the rupture load was close to one of the experimental curves when asymmetric loading was applied, as shown in Figure 24. On the other hand, in the modeling, the onset of strains occurred for higher loads, deviating from the experimental behavior. When symmetric loading was considered, the maximum strains obtained were higher than the experimental data. Moreover, it is evident that the shear reinforcement was minimally stressed, exhibiting low strains. This behavior explains why the rupture load of this model was not significantly higher than the others.

6.6 Failure surface

The failure surface was experimentally identified through a cut in the structure, conducted after the load test, only for the BD28-P2 model, as shown in Figure 25a. The experimental image clearly indicates that the main shear crack forms at the lower slab-column interface and intersects the flexural cracks in the upper region, intercepting the first and second layers of voids.

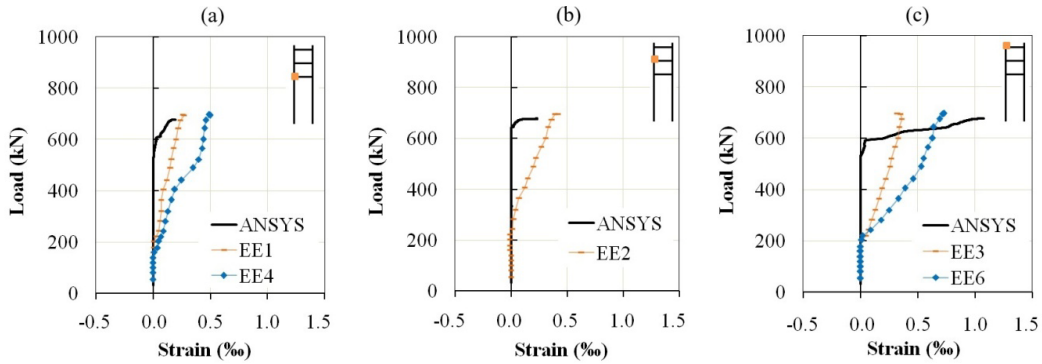

Figure 24. Strain in the punching shear reinforcement of the BD28-P3 slab.

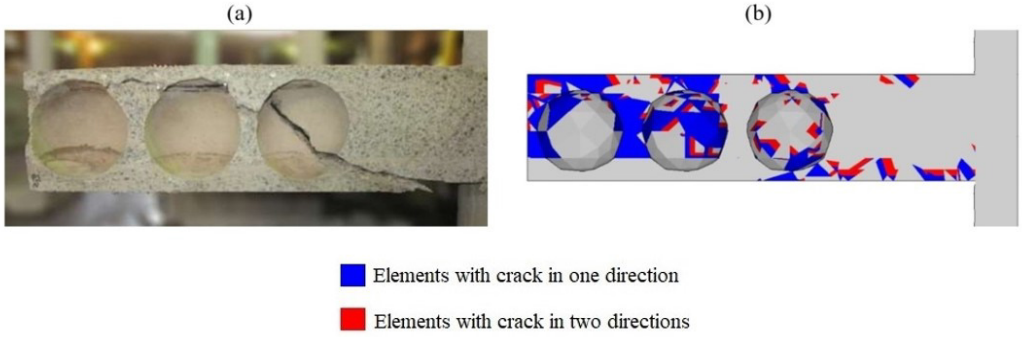

Figure 25. Failure surface of BD28-P2 slab .

In the numerical simulation, it is only possible to observe which elements have cracked in one or two directions, as shown in Figure 25b. In this case, it is evident that the modeling exhibited similar behavior, the main crack intersecting the first and second layers of voids when asymmetric loading was taken into account.

7 CONCLUSIONS

This study employed a computational FEM program to simulate the behavior of flat slabs with spherical voids. For numerical validation, experimental data from other authors, consisting of slabs subjected to asymmetric loading that failed due to punching shear, were used. The presented results demonstrated that the constitutive models considered for steel and concrete provided good predictions of experimental behavior, not only for load-displacement but also for ultimate load, load-strain, and failure surface.

When the unbalanced loads were considered, even in a simplified manner, the numerical modeling yielded results close to experimental data for both solid slab and slabs with voids models. Good approximations were observed in the load-displacement curves for the first concrete crack and stiffness for all models. In terms of ultimate loads, the results obtained were close to experimental data, with differences ranging from -0.5% to -5.86% for the RSP28, BD28-P1, and BD28-P3 models. For the BD28-P2 slab, which exhibited greater variations in load application during the test, the difference was higher, reaching +11.26%.

Good approximations to actual results were also observed in concrete and flexural reinforcement strains. Similar to the experimental data, none of the models reached the concrete crushing strain, indicating a punching shear failure. In the strains of the flexural reinforcements, it was found that only the bars positioned near the column reached the yield stress, also indicating punching shear failure in the numerical model. To ensure that the modeling presented behavior close to the experimental one, the failure surface was also analyzed, showing similar results to the experimental setup.

After validating the model for the asymmetric punching shear, interesting behaviors were observed in the symmetric case, allowing a direct comparison between the slabs. Comparing the RSP28 slab with the BD28-P1 slab, it was found that the voids in the second model reduced the ultimate load by 16.63%. Regarding the weight of the structure, the reduction is close to 28%. It was also observed that the use of a pre-slab with higher compressive strength than the rest

of the slab, model BD28-P2, does not significantly impact the ultimate load, resulting in only a 4% increase compared to the BD28-P1 model. Finally, the use of shear reinforcement in one direction had little impact on the punching shear failure of the flat slabs with voids, as the punching cone is still formed in the first layer of spheres.

Lastly, unbalanced loads make punching shear an even more critical type of failure. In the solid slab model, RSP28, considering unbalanced loads with a proportion of 0.3 between the two loads applied in the reduced numerical model (1/4 of the slab), resulted in a 13.96% reduction in the ultimate load. In the voided slab model, the unbalanced load is even more critical, with the proportion of 0.3 in the BD28-P3 slab causing a 21.27% reduction in the ultimate load compared to the symmetric case.

ACKNOWLEDGEMENTS

The authors wish to acknowledge the financial support given by the Civil Engineering Graduate Program (PPGEC) of the Federal University of Rio Grande do Sul (UFRGS) and by the Brazilian governmental research institutions CAPES and CNPQ.

REFERENCES

[1] G. R. Silva, A. Campos Fo., and M. V. Real, "Reliability of codes provisions for punching shear design," *Rev. IBRACON Estrut. Mater.*, vol. 17, no. 4, e17401, 2024, http://doi.org/10.1590/s1983-41952024000400001.

[2] M. A. Khouzani, M. Zeynalian, M. Hashemi, D. Mostofinejad, and F. Farahbod, "Investigation of flexural and shear behaviors of biaxial voided slabs containing steel cages," *Struct. Concr.*, vol. 27, pp. 1075–1085, Jul 2020, http://doi.org/10.1016/j.istruc.2020.07.017.

[3] J. H. Chung, H. S. Jung, and H. K. Choi, "Flexural strength and stiffness of donut-type voided slab," *Appl. Sci. (Basel)*, vol. 12, no. 12, pp. 5782, Jun 2022, http://doi.org/10.3390/app12125782.

[4] S. W. Han and C. S. Lee, "Evaluation of punching shear strength of voided transfer slabs," *Mag. Concr. Res.*, vol. 66, no. 21, pp. 1116–1128, Jul 2014, http://doi.org/10.1680/macr.14.00080.

[5] T. S. Al-Gasham, J. M. Mhalhal, and H. A. Jabir, "Improving punching behavior of interior voided slab-column connections using steel sheets," *Eng. Struct.*, vol. 199, pp. 109614, Sep 2019, http://doi.org/10.1016/j.engstruct.2019.109614.

[6] M. Schnellenbach-Held and K. Pfeffer, "Punching behavior of biaxial hollow slabs," *Cement Concr. Compos.*, vol. 24, no. 6, pp. 551–556, 2002, http://doi.org/10.1016/S0958-9465(01)00071-3.

[7] R. Sagadevan and B. N. Rao, "Experimental and analytical investigation of punching shear capacity of biaxial voided slabs," *Struct.*, vol. 20, pp. 340–352, Apr 2019, http://doi.org/10.1016/j.istruc.2019.03.013.

[8] J. Valivonis, T. Skuturna, M. Daugevicius, and A. Sneideris, "Punching shear strength of reinforced concrete slabs with plastic void formers," *Constr. Build. Mater.*, vol. 145, pp. 518–527, Apr 2017, http://doi.org/10.1016/j.conbuildmat.2017.04.057.

[9] N. Oukaili and H. Merie, "Reduced area approach for predicting punching shear resistance of biaxial hollow slabs with openings," *Res. Eng.*, vol. 19, pp. 1–18, Jun 2023, http://doi.org/10.1016/j.rineng.2023.101261.

[10] J. H. Chung, B. I. Bae, H. K. Choi, H. S. Jung, and C. S. Choi, "Evaluation of punching shear strength of voided slabs considering the effect of the ratio b0/d," *Eng. Struct.*, vol. 164, pp. 70–81, Mar 2018, http://doi.org/10.1016/j.engstruct.2018.02.085.

[11] M. V. Kumar and T. A. Hamza, "Finite element analysis on effect of different ball spacing in bubble deck lightweight concrete slab," *IOP Conf. Series Mater. Sci. Eng.*, vol. 872, no. 1, pp. 012124, 2020, http://doi.org/10.1088/1757-899X/872/1/012124.

[12] A. S. Mahdi and S. D. Mohammed, "Structural behavior of BubbleDeck slab under uniformly distributed load," *Civ. Eng. J.*, vol. 7, no. 2, pp. 304–319, Feb 2021, http://doi.org/10.28991/cej-2021-03091655.

[13] J. H. Chung, H. K. Choi, S. C. Lee, and C. S. Choi, "One-way shear strength of circular voided reinforced concrete floor slabs," *Proc. Inst. Civ. Eng., Struct. Build.*, vol. 168, no. 5, pp. 336–350, May 2015, http://doi.org/10.1680/stbu.14.00044.

[14] H. T. Nimnim and M. J. Z. Alabdeen, "Structural behavior of voided normal and high strength reinforced concrete slabs," *Kufa J. Eng.*, vol. 10, no. 2, pp. 1–11, 2021, http://doi.org/10.30572/2018/KJE/100201.

[15] A. M. Ibrahim, M. A. Ismael, and H. A. S. A. Hussein, "The effect of balls shapes and spacing on structural behaviour of reinforced concrete bubbled slabs," *J. Eng. Sust. Dev.*, vol. 23, no. 2, pp. 56–65, Mar 2019, http://doi.org/10.31272/jeasd.23.2.5.

[16] M. A. Khouzani, M. Zeynalian, M. Hashemi, D. Mostofinejad, and F. Farahbod, "Investigation of flexural and shear behaviors of biaxial voided slabs containing steel cages," *Struct. Concr.*, vol. 44, pp. 1–12, Oct 2019.

[17] P. V. P. Sacramento, M. P. Ferreira, D. R. C. Oliveira, and G. S. S. A. Melo, "Punching strength of reinforced concrete flat slabs without shear reinforcement," *Rev. IBRACON Estrut. Mater.*, vol. 5, no. 5, pp. 659–691, Oct 2012, http://doi.org/10.1590/S1983-41952012000500005.

[18] O. S. Paiva, M. P. Ferreira, D. R. C. Oliveira, A. F. Lima No., and M. R. Teixeira, "Influence of the column rectangularity index and of the boundary conditions in the punching resistance of slab-column connections," *Rev. IBRACON Estrut. Mater.*, vol. 8, no. 3, pp. 260–295, Jun 2015, http://doi.org/10.1590/S1983-41952015000300003.

[19] D. B. Ferreira, L. M. Trautwein, J. P. Virgens, R. B. Gomes, and L. C. Almeida, "Experimental analysis of concrete flat slabs with internal stud-type shear reinforcement," *Rev. IBRACON Estrut. Mater.*, vol. 16, no. 3, e16305, 2023, http://doi.org/10.1590/s1983-41952023000300005.

[20] J. H. Chung, H. K. Choi, S. C. Lee, and C. S. Choi, "Punching shear strength of biaxial hollow slab with donut type hollow sphere," *Key Eng. Mater.*, vol. 452, pp. 777–780, 2011, http://doi.org/10.4028/www.scientific.net/KEM.452-453.777.

[21] M. P. Ferreira, M. H. Oliveira, and G. S. S. A. Melo, "Tests on the punching resistance of flat slabs with unbalanced moments," *Eng. Struct.*, vol. 196, pp. 109311, Jul 2019, http://doi.org/10.1016/j.engstruct.2019.109311.

[22] H. J. N. Lima, "Análise experimental à punção de lajes lisas tipo Bubbledeck," Master thesis, Dept. Civ. and Env. Eng., Fed. Univ. Brasília, Brasília, 2015. http://doi.org/10.26512/2015.03.D.18978.

[23] W. G. Nicácio, "Comportamento à punção de lajes de concreto armado tipo BubbleDeck," Ph.D. dissertation, Dept. Civ. and Env. Eng., Fed. Univ. Brasília, Brasília, 2018.

[24] B. M. Lazzari, A. Campos Fo., P. M. Lazzari, and A. R. Pacheco, "Using element-embedded rebar model in ANSYS for the study of reinforced and prestressed concrete structures," *Comput. Concr.*, vol. 19, no. 4, pp. 347–356, Apr 2017, http://doi.org/10.12989/cac.2017.19.4.347.

[25] P. M. Lazzari, A. Campos Fo., P. M. Lazzari, A. R. Pacheco, and R. Gomes, "Numerical simulation of the constructive steps of a cable-stayed bridge using ANSYS," *Struct. Eng. Mech.*, vol. 69, pp. 269–281, Feb 2019, http://doi.org/10.12989/sem.2019.69.3.269.

[26] I. S. Hoffman, B. M. Lazzari, A. Campos Fo., P. M. Lazzari, and A. R. Pacheco, "Finite element numerical simulation of a cable-stayed bridge construction through the progressive cantilever method," *Struct. Concr.*, vol. 23, no. 2, pp. 632–651, Feb 2022, http://doi.org/10.1002/suco.202100662.

[27] G. G. Machado, A. Campos Fo., P. M. Lazzari, B. M. Lazzari, and A. R. Pacheco, "Numerical simulation by the finite element method of the constructive steps of a precast prestressed segmental bridge," *Struct. Eng. Mech.*, vol. 85, no. 2, pp. 163–177, Jan 2023, http://doi.org/10.1002/suco.202100662.

[28] P. B. Soares, P. M. Lazzari, A. Campos Fo., B. M. Lazzari, and A. R. Pacheco, "Identification of the failure modes of CFRP shear-strengthened reinforced concrete beams by the finite element method," *Rev. IBRACON Estrut. Mater.*, vol. 16, no. 3, e16304, 2023, http://doi.org/10.1590/s1983-41952023000300004.

[29] N. S. Ottosen, "A failure criterion for concrete," *J. Eng. Mech. Div.*, vol. 103, no. 4, pp. 527–535, 1977, http://doi.org/10.1061/JMCEA3.0002248.

[30] Fédération Internationale du Béton, *fib Model Code for Concrete Structures 2010.* Lausanne: *fib*, 2013.

[31] M. Cervera, E. Hinton, J. Bonet, and N. Bicanic, "Nonlinear transient dynamic analysis of three-dimensional structures: a finite element program for steel and reinforced concrete materials," in *Numerical Methods and Software for Dynamic Analysis of Plates and Shells*, E. Hinton, Ed., Swansea, UK: Pineridge Press Limited, 1988, ch. 7, pp. 320–504.

[32] Comité Euro-International du Béton, *Concrete Under Multiaxial States of Stress: Constitutive Equations for Practical Design* (Bulletin D'information 156). Lausanne: CEB, 1983.

[33] Comité Euro-International du Béton, *CEB-FIP Model Code 1990, Final Draft*. Lausanne: CEB, 1991.

[34] F. M. Quevedo, R. J. Schmitz, I. B. Morsch, A. Campos Fo, and D. B. Maghous, "Customization of a software of finite elements to analysis of concrete structures: long-term effects," *Rev. IBRACON Estrut. Mater.*, vol. 11, no. 4, pp. 696–718, 2018, http://doi.org/10.1590/s1983-41952018000400005.

[35] K. J. Bathe, *Finite Element Procedures*. Upper Saddle River: Prentice Hall, 1996.

[36] ANSYS Inc, *ANSYS help system version 21.2.* Canonsburg: ANSYS Inc., 2018.

Author contributions: ERZS: conceptualization, writing, data curation, formal analysis, and methodology; ACF, BML and PML: conceptualization, formal analysis, methodology, and supervision.

Editors: Leandro Trautwein, Daniel Carlos Taissum Cardoso.